

# Noble-Metal-Free Ni–W–O-Derived Catalysts for High-Capacity Hydrogen Production from Hydrazine Monohydrate

Qing Shi, Deng-Xue Zhang, Hui Yin, Yu-Ping Qiu, Liang-Liang Zhou, Chen Chen, Hui Wu, and Ping Wang\*

Cite This: *ACS Sustainable Chem. Eng.* 2020, 8, 5595–5603

Read Online

ACCESS |

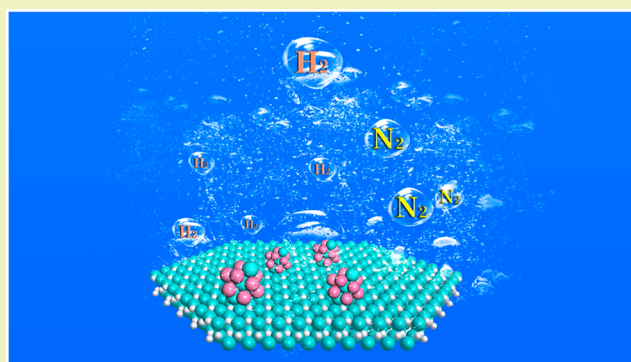
Metrics & More

Article Recommendations

Supporting Information

**ABSTRACT:** Development of active and earth-abundant catalysts is pivotal to render hydrazine monohydrate ( $\text{N}_2\text{H}_4\cdot\text{H}_2\text{O}$ ) viable as a hydrogen carrier. Herein, we report the synthesis of noble-metal-free Ni–W–O-derived catalysts using a hydrothermal method in combination with reductive annealing treatment. Interestingly, the thus-prepared Ni-based catalysts exhibit remarkably distinct catalytic properties toward  $\text{N}_2\text{H}_4\cdot\text{H}_2\text{O}$  decomposition depending upon the annealing temperature. From a systematic phase/microstructure/chemical state characterization and the first-principles calculations, we found that the variation of the apparent catalytic properties of these Ni-based catalysts should stem from the formation of different Ni–W alloys with distinct intrinsic activity, selectivity, and distribution state. The thereby chosen Ni–W alloy nanocomposite catalyst prepared under an optimized condition showed high activity, nearly 100% selectivity, and excellent stability toward  $\text{N}_2\text{H}_4\cdot\text{H}_2\text{O}$  decomposition for hydrogen production. Furthermore, this noble-metal-free catalyst enables rapid hydrogen production from commercially available  $\text{N}_2\text{H}_4\cdot\text{H}_2\text{O}$  solution with an intriguingly high hydrogen capacity of 6.28 wt % and a satisfactory dynamic response property. These results are inspiring and momentous for promoting the use of the  $\text{N}_2\text{H}_4\cdot\text{H}_2\text{O}$ -based  $\text{H}_2$  source systems.

**KEYWORDS:** *Hydrogen storage, Hydrazine monohydrate, Noble-metal-free catalyst, Ni–W alloy, Phase evolution*



## INTRODUCTION

Hydrogen is expected to play an essential role as an energy carrier in the future clean energy economy based on renewable energy resources. However, the widespread utilization of hydrogen is hampered by the technical difficulty involved in hydrogen storage and delivery.<sup>1</sup> The materials capable of reversible dehydrogenation have long been sought as possible candidates for high-capacity hydrogen storage.<sup>2–13</sup> However, none of the existing materials met the requirements for hydrogen capacity (over 6 wt %), kinetics, and operation temperature. Recently, chemical hydrogen storage involving hydrolysis or thermolysis of hydrogen-rich materials and spent-fuel regeneration has emerged as a competitive alternative to a high-pressure hydrogen cylinder for vehicular and portable applications.<sup>14,15</sup> Among the hydrogen-rich materials of interest, hydrazine monohydrate ( $\text{N}_2\text{H}_4\cdot\text{H}_2\text{O}$ ) is an appealing candidate thanks to its favorable combination of low cost, high hydrogen capacity (8.0 wt %), and good stability at ambient temperatures.<sup>16,17</sup> In particular, the decomposition reactions of  $\text{N}_2\text{H}_4$  yield only gaseous products, which is highly beneficial for the design and practical application of  $\text{H}_2$ -source systems.

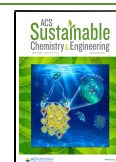
The development of  $\text{N}_2\text{H}_4\cdot\text{H}_2\text{O}$  as a chemical hydrogen storage material requires highly active and selective catalysts

for promoting hydrogen production (HP), and meanwhile suppressing the formation of  $\text{NH}_3$ . In the past decades, a number of transition metals/alloys have been investigated in terms of catalytic properties toward  $\text{N}_2\text{H}_4\cdot\text{H}_2\text{O}$  decomposition.<sup>18–47</sup> It was found that alloying is a highly effective approach for boosting the catalytic performance toward HP from  $\text{N}_2\text{H}_4\cdot\text{H}_2\text{O}$ . The alloying aspect could be understood from two complementary effects: the geometric and electronic modifications of the catalyst surface.<sup>29,31</sup> The bimetallic alloys composed of a combination of precious metals (like Pt and Ir) and nonprecious metals (like Ni, Co, and Fe) generally exhibited favorable performance in both activity and  $\text{H}_2$  selectivity.<sup>20–24,28–33,39–42</sup> In contrast, the catalytic activity of the noble-metal-free alloys is typically inferior. For instance, the reaction rates of  $\text{N}_2\text{H}_4\cdot\text{H}_2\text{O}$  decomposition over the representative Ni-based catalysts, such as NiCu/CeO<sub>2</sub>, NiFe/

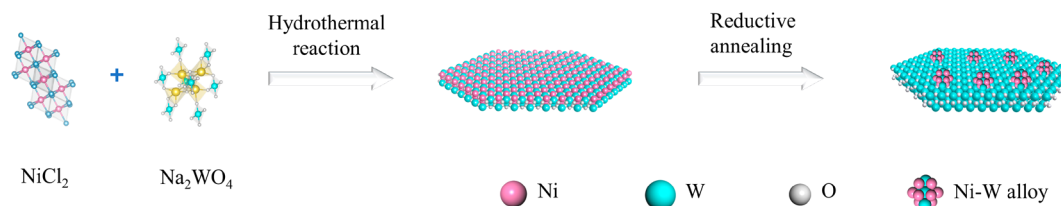
Received: December 28, 2019

Revised: March 15, 2020

Published: March 23, 2020



Scheme 1. Schematic Diagram of the Fabrication Process of the Ni–W–O-Derived Nanocatalysts



$\text{CeO}_2$ ,  $\text{NiCo/NiO-CoO}_x$ , and  $\text{NiMo/NiMoO}$ , were 1 or 2 orders of magnitude lower than those of the  $\text{NiPt}$  and  $\text{CoPt}$  catalysts.<sup>27,37,43–46</sup> Currently, the less favorable modification effects of non-precious metals compared to noble metals are still poorly understood, but from the perspectives of the cost reduction and growth potential, non-precious-metal catalysts represent an important direction for future research of the  $\text{N}_2\text{H}_4\cdot\text{H}_2\text{O}$ -based HP technology. In general, activity improvement of non-precious-metal catalysts can be pursued via composition/phase tuning and structure optimization. In this regard, in-depth study and better understanding of the phase–microstructure–activity correlation are clearly of significance for the design and synthesis of advanced catalysts. In addition, stability is a key issue in the study of the catalyst toward  $\text{N}_2\text{H}_4\cdot\text{H}_2\text{O}$  decomposition. The existing  $\text{N}_2\text{H}_4\cdot\text{H}_2\text{O}$  decomposition catalysts from the literature all suffered from serious activity loss in cyclic usage. Currently, the mechanistic reasons for the poor stability remain unclear. Possible factors influencing the stability of  $\text{N}_2\text{H}_4\cdot\text{H}_2\text{O}$  decomposition catalysts include particle agglomeration, subtle phase transformation, and strong binding of the products and/or intermediates on the catalyst surface.<sup>27,39,47</sup>

We herein report the synthesis of a Ni–W–O-derived nanocatalyst toward HP from  $\text{N}_2\text{H}_4\cdot\text{H}_2\text{O}$  using a hydrothermal method in combination with reductive annealing. The catalyst prepared under optimal conditions showed excellent activity, nearly 100% selectivity, and exceptionally high stability in catalyzing  $\text{N}_2\text{H}_4\cdot\text{H}_2\text{O}$  decomposition for HP. A combination of experimental and theoretical investigations was conducted to probe the temperature-dependent evolutions of the phase structures and microstructural features, and to reveal their correlation with the catalytic properties.

## EXPERIMENTAL SECTION

**Chemicals and Catalyst Synthesis.** Nickel chloride hexahydrate ( $\text{NiCl}_2\cdot 6\text{H}_2\text{O}$ , 98%), sodium tungstate dihydrate ( $\text{Na}_2\text{WO}_4\cdot 2\text{H}_2\text{O}$ , 99.5%), ethanol ( $\text{C}_2\text{H}_5\text{OH}$ , 99.7%), sodium hydroxide ( $\text{NaOH}$ , 98%), and hydrazine monohydrate ( $\text{N}_2\text{H}_4\cdot\text{H}_2\text{O}$ , 98%) were obtained from commercial sources and used as-received. Deionized (DI) water and  $\text{C}_2\text{H}_5\text{OH}$  were used for preparation of all aqueous solutions.

The target catalyst was synthesized by a two-step procedure involving hydrothermal reaction and subsequent annealing treatment under a reductive atmosphere. In a typical run, 2 mmol of  $\text{Na}_2\text{WO}_4\cdot 2\text{H}_2\text{O}$  was dissolved into 20 mL of DI water, followed by dropwise addition of an equal portion of  $\text{NiCl}_2\cdot 6\text{H}_2\text{O}$  aqueous solution. This process was operated under magnetic stirring, typically for 20 min. The obtained green milky suspension was transferred to a stainless steel autoclave (50 mL) and kept at 160 °C for 6 h. The sample was collected after cooling to ambient temperature and was sequentially washed with DI water and  $\text{C}_2\text{H}_5\text{OH}$  and then vacuum-dried at 60 °C for 2 h. The thus-prepared sample was subsequently annealed at different temperatures (350, 400, and 600 °C) under a flowing  $\text{H}_2$  atmosphere for 2 h.

**Characterization of the Catalysts.** The phase, composition, and structure of the as-prepared materials were characterized by X-ray

diffraction (XRD, Rigaku RINT 2000 using  $\text{Cu K}\alpha$  monochromatized radiation), transmission electron microscopy (TEM, JEOL-2100F), Fourier transform infrared spectroscopy (FTIR, Nicolet IS10), Raman spectroscopy (Thermo Scientific DXR with an excitation wavelength of 532 nm), and X-ray photoelectron spectroscopy (XPS, Thermo Scientific K-ALPHA+ using an  $\text{Al K}\alpha$  X-ray source). In the analysis of XPS results, the C 1s signal at 284.8 eV of adventitious carbon was used for calibration of the binding energy scale. The XPS PEAK 4.1 software was used for curve fitting. The  $\text{N}_2$  adsorption/desorption isotherm measurements were conducted in a Micromeritics ASAP 2460 apparatus. The postused fuel solution was examined by ultraviolet–visible spectroscopy (UV–vis, Thermo Scientific Evolution 220) to determine whether or not hydrazine had completely decomposed.

**Catalytic Performance Testing.** The catalytic decomposition properties of dilute  $\text{N}_2\text{H}_4\cdot\text{H}_2\text{O}$  solution was examined in a two-necked round-bottomed flask with an external heating apparatus. In a typical run, the flask containing the catalyst and an alkaline aqueous solution was preheated at the desired temperature under magnetic stirring. After injection of  $\text{N}_2\text{H}_4\cdot\text{H}_2\text{O}$  into the flask, the decomposition reaction immediately occurred. The generated gaseous products passed through a 1.0 M hydrochloric acid solution to absorb ammonia, if any, and then were measured by the water-displacement method using an electronic balance with a precision of  $\pm 0.01$  g.

In the test of the catalytic decomposition properties of concentrated  $\text{N}_2\text{H}_4\cdot\text{H}_2\text{O}$  solution, an online mass flowmeter equipped with a silica drier (Seven-star Huachang CS 200,  $\pm 1\%$  precision) was used to monitor the volume of the gaseous products. Each experiment was repeated at least twice to minimize the measurement error (no more than  $\pm 2\%$ ).

The reaction rate was evaluated at a reactant conversion of 50%, assuming all the Ni atoms take part in the catalytic reaction.<sup>22,31</sup> Here, because of the time dependence of the reactivity rate, the standard choice of the reaction time parameter is important for rationally comparing the activities of different catalysts. The selectivity toward HP ( $X$ ) was determined by eq 1. The details about its derivation can be found in ref 31.

$$X = \frac{3Y - 1}{8} \left[ Y = \frac{n(\text{N}_2 + \text{H}_2)}{n(\text{N}_2\text{H}_4)} \right] \quad (1)$$

**Computational Methods.** Density functional theory (DFT) calculations were performed using the Vienna Ab Initio Simulation Package (VASP 5.2).<sup>48</sup> The Perdew–Burke–Ernzerhof exchange–correlation functional of the generalized gradient approximation and the projector augmented-wave pseudopotential were used to describe the core electrons and the electron interactions, respectively.<sup>49,50</sup> A plane-wave cutoff energy was taken to be 500 eV and the Brillouin zone was sampled with a  $5 \times 5 \times 1$  mesh. The van der Waals interactions were taken into account using Grimme’s DFT-D2 method.<sup>51,52</sup> The structure was fully optimized until all forces acting on atoms were less than 0.02 eV/Å.

The  $\text{Ni}_{17}\text{W}_3(111)$  and  $\text{Ni}_4\text{W}(211)$  surfaces were modeled by  $(2\sqrt{3} \times 2\sqrt{3})$  and  $(1 \times 1)$  five-layer slabs, respectively. Because both  $\text{Ni}_{17}\text{W}_3$  and Ni belong to the same space group ( $Fm\bar{3}m$ , No. 255), the  $\text{Ni}_{17}\text{W}_3(111)$  surface was simulated by a Ni(111) slab with 9 Ni atoms substituted by 9 W atoms in agreement with the ratio of Ni to

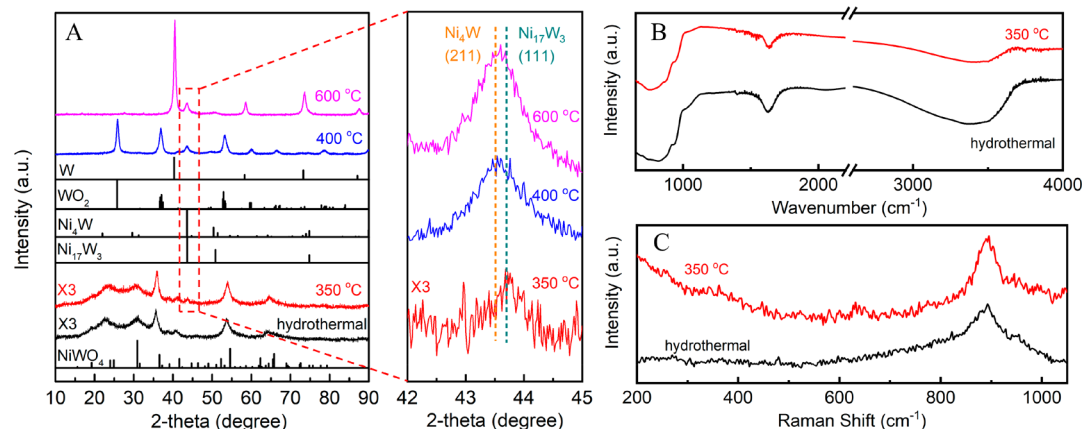


**Figure 1.** (A) XRD patterns of various samples. (B) FTIR and (C) Raman spectra of hydrothermal and 350 °C-reduced sample.

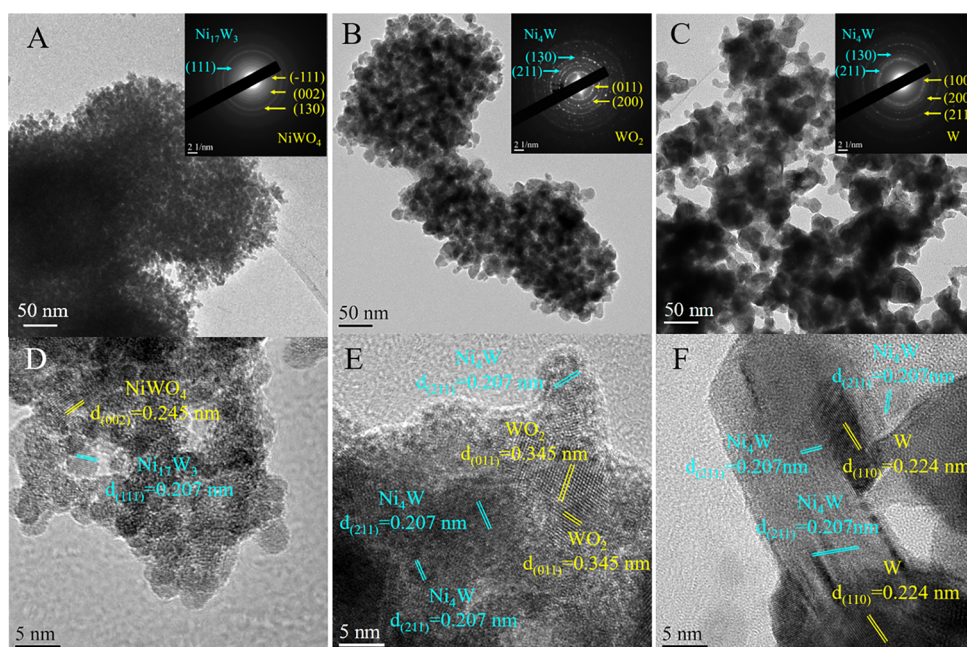


**Figure 2.** TEM and HRTEM images of the catalysts reduced at (A, D) 350 °C, (B, E) 400 °C, and (C, F) 600 °C. The insets showed the corresponding SAED patterns of the catalysts.

W atoms (17:3). Periodic images were separated by a vacuum region of 15 Å in the *z* direction (Figure S1, Supporting Information).

The adsorption energies of  $N_2H_4$  ( $E_{ads}$ ) were calculated as

$$E_{ads} = E_{X/surf} - E_{surf} - E_X \quad (2)$$

where  $E_X$  and  $E_{surf}$  represent the energies of  $N_2H_4$  in the gas phase and the clear surfaces, respectively.  $E_{X/surf}$  is the total energy of the surface with an adsorbed  $N_2H_4$  molecule.

## RESULTS AND DISCUSSION

The Ni–W–O-derived nanocatalyst was prepared by a two-step procedure, as illustrated in Scheme 1. First, a nickel tungsten oxide precursor was synthesized via a simple hydrothermal process. The thus-synthesized sample was then calcined at elevated temperature under an  $H_2$  atmosphere to obtain the target catalyst. The XRD pattern of the as-synthesized hydrothermal sample (Figure 1A) resembles some features of that of  $NiWO_4$  but with significant peak broadening and diffuse scattering, indicating the formation of a poorly crystallized product. Further annealing this sample at elevated

temperature (over 400 °C) in air could help remove possible solvent residue, improve its crystallinity, promote crystallite growth, and result in a well-defined XRD pattern consistent with that of  $NiWO_4$  (JCPDS 15-0755) (Figure S2, Supporting Information). Because of the poor crystallinity nature of the as-synthesized hydrothermal sample, its phase assignment was further corroborated by the spectroscopic analyses. FTIR spectra of the hydrothermal sample (Figure 1B) exhibited an intense peak at  $822\text{ cm}^{-1}$  corresponding to the stretching vibrations of O–W–O.<sup>53,54</sup> And the IR bands at around 1650 and  $3400\text{ cm}^{-1}$  in Figure 1B should be assigned to the OH bending and stretching vibrations of the adsorbed water molecules. The Raman spectrum (Figure 1C) clearly showed a strong band at  $883\text{ cm}^{-1}$ , which should be ascribed to the stretching vibrational mode of terminal W=O bonds, consistent with the featured assembly of  $WO_6$  octahedra in the  $NiWO_4$  structure.<sup>53,54</sup>

Reductive annealing the hydrothermal sample at various temperatures resulted in the formation of nanocomposite catalysts with varied phase compositions and structures. As

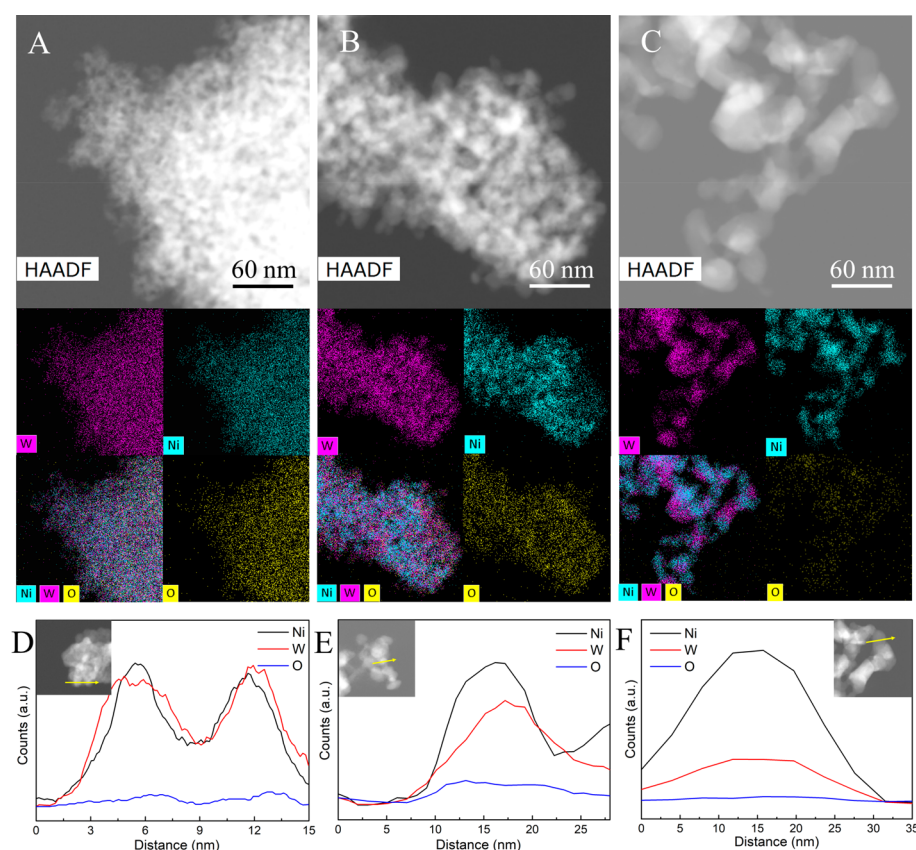


**Figure 3.** HAADF-STEM images and the corresponding EDS maps of the reduced catalysts at 350 °C (A), 400 °C (B), and 600 °C (C). The EDS line-scanning profiles of the reduced samples at 350 °C (D), 400 °C (E), and 600 °C (F).

shown in Figure 1A, the 350 °C-reduced sample showed a similar XRD pattern to that of the hydrothermal sample but with a new peak appearing at  $2\theta = 43.68^\circ$ , matching well with the (111) peak of the  $\text{Ni}_{17}\text{W}_3$  phase (JCPDS 65-4828). Upon increasing the annealing temperature to 400 °C, this peak becomes intensified with a low-angle shift by  $0.2^\circ$ , which corresponds well to the (211) peak of the  $\text{Ni}_4\text{W}$  phase (JCPDS 65-2673). Meanwhile, the diffraction peaks from the hydrothermal sample completely disappeared and were replaced by the characteristic peaks from the  $\text{WO}_2$  phase (JCPDS 32-1393). With further elevation of the annealing temperature to 600 °C,  $\text{WO}_2$  was reduced to metal W (JCPDS 04-0806) but with the  $\text{Ni}_4\text{W}$  phase still preserved. The phase assignments of the 400- and 600 °C-reduced samples were further supported by the Raman spectra (Figure S3, Supporting Information).

Phase structure evolution of the hydrothermal samples upon reductive annealing was further investigated by operating TEM in high-resolution and selected-area electron diffraction (SAED) modes. As shown in Figure 2A–C, the SAED patterns discern the evolutionary reduction of the small  $\text{NiWO}_4$  crystallites in the hydrothermal sample during the reductive annealing process, from the initial precipitation of  $\text{Ni}_{17}\text{W}_3$  to the concurrent formation of  $\text{Ni}_4\text{W}$  and  $\text{WO}_2$ , and further to the metallic  $\text{Ni}_4\text{W}$  and W phases. The high-resolution TEM images reveal the microstructure and phase constitution of the reduced samples. In the 350 °C-reduced sample, the lattice fringes with interplanar distances of 0.207 and 0.245 nm could be assigned to the (111) plane of  $\text{Ni}_{17}\text{W}_3$  and the (002) plane of  $\text{NiWO}_4$ , respectively (Figure 2D). Similarly, the characteristic  $d$ -spacings from the crystalline  $\text{Ni}_4\text{W}$  and  $\text{WO}_2$  nanoparticles were identified in the 400 °C-

reduced sample (Figure 2E). Compared to the  $\text{Ni}_{17}\text{W}_3$  phase in the 350 °C-reduced sample,  $\text{Ni}_4\text{W}$  nanoparticles showed both increased amount and particle size, consistent with the XRD results. In the 600 °C-reduced sample (Figure 2F), the lattice fringes with an interplanar distance of 0.224 nm can be safely assigned to the (110) plane of the W phase, and the dispersion of  $\text{Ni}_4\text{W}$  nanoparticles on the W substrate was clearly evidenced. In addition, some disordered domains were also observed, indicating the presence of amorphous phase in these reduced samples at different temperatures. In an effort to determine how the Ni–W alloy phases distribute on the W-containing substrates, we examined the reduced samples by high-angle annular dark-field scanning transmission electron microscopy (HAADF-STEM) in combination with energy X-ray dispersive spectroscopy (EDS) analysis. As shown in Figure 3A–C, the Ni and W elemental distributions gradually change from the atomic dispersion to the segregated nanoclusters with increasing annealing temperature. For the 400 °C-reduced sample, the segregation of Ni and W elements became detectable because of the formation of the distinct  $\text{Ni}_4\text{W}$  and  $\text{WO}_2$  phases. Further increasing the annealing temperature to 600 °C resulted in aggravated segregation Ni and W, owing to the formation of W and the particle growth and aggregation of  $\text{Ni}_4\text{W}$ . A close examination of the samples by EDS line-scanning profile analysis (Figure 3D–F) suggested that the size of the  $\text{Ni}_4\text{W}$  nanoparticles increased from around 15 to 30 nm upon elevation of the annealing temperature from 400 to 600 °C.

The chemical states of the constituent elements in the hydrothermal and reduced samples were also examined using the surface-sensitive XPS. As presented in Figure 4, the

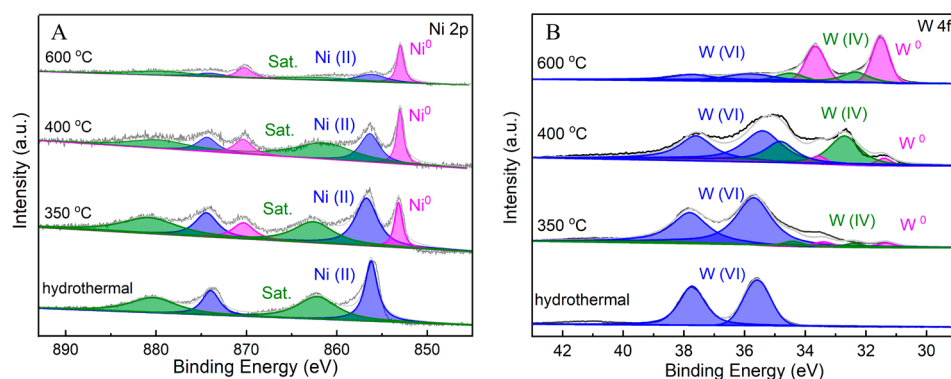


**Figure 4.** XPS results of the hydrothermal and reduced samples: (A) Ni 2p spectra and (B) W 4f spectra.

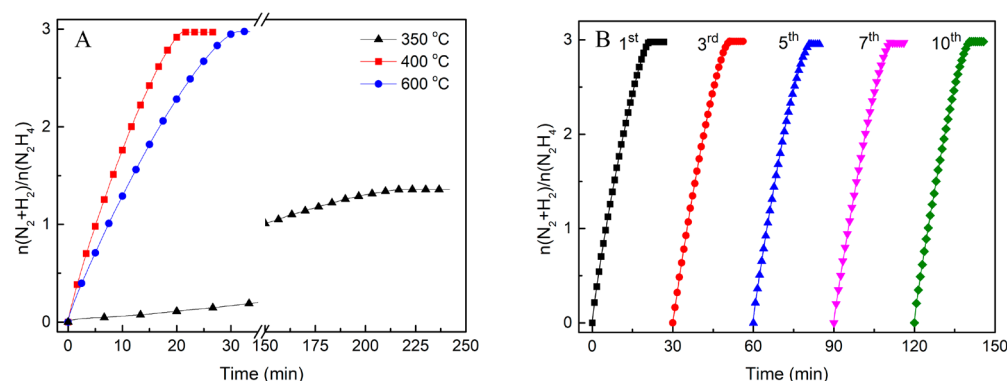


**Figure 5.** Kinetic curves of  $\text{N}_2\text{H}_4\cdot\text{H}_2\text{O}$  decomposition over the reduced catalysts at different temperatures. (B) Cyclic performance of the 400 °C-reduced catalyst. (reaction conditions: 2 mL solution composed of 0.5 M  $\text{N}_2\text{H}_4\cdot\text{H}_2\text{O}$  and 2.0 M NaOH at 50 °C, catalyst/ $\text{N}_2\text{H}_4\cdot\text{H}_2\text{O}$  = 1:20).

hydrothermal sample exhibited only Ni(II) and W(VI) signals. After the reductive annealing treatment, additional signals of metallic Ni<sup>0</sup> were detected, and their intensities increase with increasing annealing temperature. Similarly, the W 4f spectra of the reduced samples clearly manifested the formation of W(IV) and W<sup>0</sup> species upon reduction. These results were in accord with XRD, SAED, and HRTEM observations, supporting the evolutionary formation of Ni–W alloys and W-containing substrate phases during the reduction process. A close examination of the XPS spectra further found subtle but significant binding energy (BE) shifts of Ni<sup>0</sup> and W<sup>0</sup>. Specifically, the BEs of Ni<sup>0</sup> in the reduced samples were observed to negatively shift in comparison with the BE of pristine metal Ni at 853.3 eV. Meanwhile, the W<sup>0</sup> in the reduced samples showed positive BE shifts relative to pure W (31.0 eV). These results clearly indicated the electron transfer from W to Ni as a consequence of Ni–W alloys formation.<sup>22–24,37,55</sup> In addition, XPS analysis clearly detected Ni(II) and W(VI) signals throughout the reduced samples but with decreased intensities upon high-temperature annealing. These results, together with the XRD, Raman, and HRTEM characterizations (Figure 1A, Figure 2F, and Figure S3), suggested the presence of NiWO<sub>4</sub> and WO<sub>3–x</sub> amorphous phases in the reduced samples. On the basis of the combination of phase, microstructure, and chemical state analyses, the resulting nanocatalysts from reductive annealing of the NiWO<sub>4</sub> precursor at different temperatures were denoted as Ni<sub>1.7</sub>W<sub>3</sub>/NiWO<sub>4</sub> (350 °C), Ni<sub>4</sub>W/WO<sub>2</sub>/NiWO<sub>4</sub> (400 °C), and Ni<sub>4</sub>W/W/WO<sub>3–x</sub> (600 °C), respectively.

Catalytic properties toward  $\text{N}_2\text{H}_4\cdot\text{H}_2\text{O}$  decomposition were then studied on these Ni–W–O-derived nanocomposite

catalysts. According to control experiments, changing the molar ratio of Ni/W precursors caused a variation of catalytic properties toward  $\text{N}_2\text{H}_4\cdot\text{H}_2\text{O}$  decomposition, and the optimal Ni/W precursors molar ratio was determined to be 1/1 (Figure S4, Supporting Information). Additionally, it was found that the reductive annealing temperature exerted significant influence on the catalytic properties of the resulting catalyst. As presented in Figure 5A, the 350 °C-reduced catalyst showed a very low reaction rate of 2 h<sup>-1</sup> and a poor H<sub>2</sub> selectivity of only 25%. In sharp contrast, the 400 °C-reduced catalyst exhibited a higher rate of 33 h<sup>-1</sup> and a H<sub>2</sub> selectivity of 99%, which enabled a complete decomposition of  $\text{N}_2\text{H}_4\cdot\text{H}_2\text{O}$  at 50 °C within 18 min. Further increasing the annealing temperature, however, seems to deteriorate the reaction rate, from 33 to 28 h<sup>-1</sup>. We then investigated the drastic changes of the apparent catalytic properties of these nanocomposite catalysts from the aspects of investigating the intrinsic catalytic properties, comparing the number of active sites and understanding the metal–support interactions. For the different catalytic properties of the 350- and 400 °C-reduced samples, we first examined and compared their specific surface areas (SSA) using N<sub>2</sub> adsorption/desorption method. It was found that increasing the annealing temperature from 350 to 400 °C resulted in a decrease of SSA from 76.2 to 30.9 m<sup>2</sup> g<sup>-1</sup> (Figure S5, Supporting Information), which was contrary to their catalytic property improvements. We then conducted control experiments to evaluate the possible effect of support materials on the catalytic properties via metal–support interactions. Specifically, we fixed the annealing temperature at 350 °C and examined the annealing time dependence of phase structure and catalytic properties. It was found that

prolongation of annealing time from 2 to 5 h caused no appreciable change of NiWO<sub>4</sub> substrate phase but resulted in the formation of Ni<sub>4</sub>W instead of Ni<sub>17</sub>W<sub>3</sub> phase (Figure S6, Supporting Information). A property test found that the 5-h-reduced sample (350 °C) showed an over 9 times increase of activity and an increase of H<sub>2</sub> selectivity from 25% to 87% compared to the 2-h-reduced sample (350 °C). The catalytic activity and H<sub>2</sub> selectivity of the 5-h-reduced sample (350 °C) were even comparable to those of the 400 °C-reduced catalyst, which was composed of Ni<sub>4</sub>W, WO<sub>2</sub>, and NiWO<sub>4</sub> amorphous phases (Figure S7, Supporting Information). These results suggested that the substrate phase did not play an important role in the present system, and the observed catalytic property differences between the 350- and 400 °C-reduced samples should be attributed to the variation of the active phases. The different catalytic behaviors of the Ni<sub>4</sub>W and Ni<sub>17</sub>W<sub>3</sub> phase were further evaluated and supported by our first-principle calculations as stated below. For the catalytic property differences of the 400- and 600 °C-reduced samples, we noticed that the two catalysts shared a common Ni<sub>4</sub>W active phase, and metallic W was experimentally demonstrated to be inactive toward N<sub>2</sub>H<sub>4</sub>·H<sub>2</sub>O decomposition. Therefore, the activity degradation of the 600 °C-reduced sample might stem from the particle growth and aggregation of the Ni<sub>4</sub>W species at elevated temperatures, as evidenced by the increased Ni–W alloy particle size observed in EDS line-scanning profile analysis (Figure 3E,F). In addition, the N<sub>2</sub> adsorption/desorption isotherm measurements revealed that the SSAs of the catalyst samples decreased from 30.9 to 12.6 m<sup>2</sup> g<sup>-1</sup> upon increasing the annealing temperature from 400 to 600 °C (Figure S5, Supporting Information).

To gain more insight into the catalytic properties of the Ni–W–O-derived catalysts, we conducted DFT calculations to investigate the activities and selectivities of Ni<sub>4</sub>W and Ni<sub>17</sub>W<sub>3</sub> alloys. On the basis of the bond-order conservation principle, we adopted the adsorption strengths of N<sub>2</sub>H<sub>4</sub> on the metallic surfaces as an indicator of the activity toward N<sub>2</sub>H<sub>4</sub> decomposition.<sup>56,57</sup> As seen in Figure 6, the most stable adsorption conformation of N<sub>2</sub>H<sub>4</sub> was one-N-atom conformation on the Ni atom of both surfaces (for details, see Figure S8, Supporting Information). The adsorption strength of N<sub>2</sub>H<sub>4</sub> was enhanced on the Ni<sub>4</sub>W surface as compared to that on the

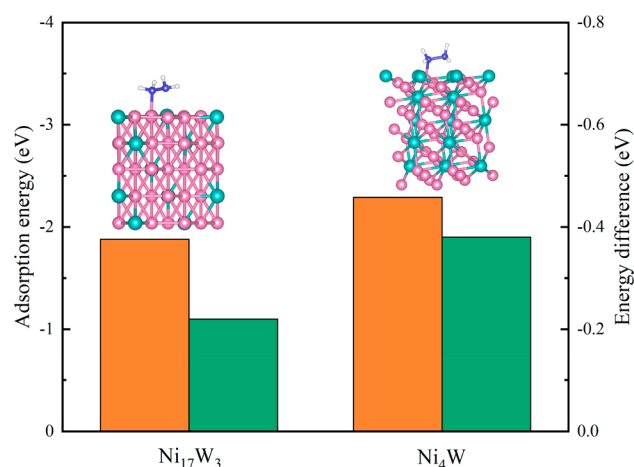


**Figure 6.** Adsorption energy (orange) of N<sub>2</sub>H<sub>4</sub> and the adsorption energy difference (olive) between one-N-atom and two-N-atom adsorption configurations on Ni<sub>17</sub>W<sub>3</sub> (111) and Ni<sub>4</sub>W (211) surfaces.

Ni<sub>17</sub>W<sub>3</sub> surface, suggesting a higher activity of Ni<sub>4</sub>W toward N<sub>2</sub>H<sub>4</sub> dissociation than Ni<sub>17</sub>W<sub>3</sub>. This may well account for the experimentally observed activity change of the 350- and 400 °C-annealed samples. With respect to the selectivity, a fundamental understanding of adsorption and decomposition behaviors of N<sub>2</sub>H<sub>4</sub> over metal surfaces is required to identify a suitable indicator for the complex multiparametric system. Previous studies illustrated that different initial adsorption conformations of N<sub>2</sub>H<sub>4</sub> over metal surfaces can lead to distinct reaction pathways.<sup>58–60</sup> In the case of only one N atom of N<sub>2</sub>H<sub>4</sub> bonded to the metal surfaces, N–H bond cleavage of N<sub>2</sub>H<sub>4</sub> molecules is energetically more favorable than N–N bond cleavage, which preferably results in H<sub>2</sub> production. In contrast, the adsorption conformation with both N atoms of N<sub>2</sub>H<sub>4</sub> bonding to the surfaces dominantly leads to NH<sub>3</sub> formation. Hence, the adsorption energy difference between one-N-atom and two-N-atom conformations can serve as an indicator to evaluate the reaction selectivity of N<sub>2</sub>H<sub>4</sub> decomposition. According to the DFT calculation results, the adsorption energy difference on the Ni<sub>4</sub>W surface is larger than that on the Ni<sub>17</sub>W<sub>3</sub> surface by nearly a factor of 2, implying a significantly higher H<sub>2</sub> selectivity for Ni<sub>4</sub>W. This is in good accordance with the experimental results. Therefore, it can be concluded that the improved catalytic performance of the Ni–W–O-derived catalysts upon increasing the annealing temperature from 350 to 400 °C should stem from the resultant Ni<sub>4</sub>W with higher intrinsic activity and H<sub>2</sub> selectivity than Ni<sub>17</sub>W<sub>3</sub>.

Next, we focused on the best-performing 400 °C-reduced catalyst sample for a detailed property test. We first inspected its stability as the poor stability is a common and critical problem for the N<sub>2</sub>H<sub>4</sub>·H<sub>2</sub>O decomposition catalysts. In the present study, the newly developed Ni<sub>4</sub>W/WO<sub>2</sub>/NiWO<sub>4</sub> nanocomposite catalyst was found to exhibit surprisingly high stability. For instance, the catalyst showed no appreciable decay of activity and H<sub>2</sub> selectivity after 10 cycles of use (Figure 5B), which were unprecedentedly better than the performance of N<sub>2</sub>H<sub>4</sub>·H<sub>2</sub>O decomposition catalysts hitherto reported (Table S1, Supporting Information). XRD and TEM analyses of the 400 °C-reduced catalyst after 10 cycles of use show no significant change in morphology, microstructure, and phase structure (Figures S9 and S10, Supporting Information), suggesting high stability of the Ni–W–O-derived catalyst. The mechanism of the excellent stability of the present Ni<sub>4</sub>W/WO<sub>2</sub>/NiWO<sub>4</sub> nanocomposite catalyst is still under investigation. A high-capacity HP system consisting of the commercial 98 wt % N<sub>2</sub>H<sub>4</sub>·H<sub>2</sub>O (17.5 M) solution and NaOH (2.0 M) promoter was employed by using this catalyst. As shown in Figure 7A, the decomposition reaction of N<sub>2</sub>H<sub>4</sub>·H<sub>2</sub>O was immediately triggered with no appreciable lag time when the Ni<sub>4</sub>W/WO<sub>2</sub>/NiWO<sub>4</sub> catalyst contacted the fuel solution. The reaction rate of the system rapidly reached its maximum (90 mL (N<sub>2</sub> + H<sub>2</sub>) min<sup>-1</sup>) within ~1 min and maintained at a level of ~80 mL (N<sub>2</sub> + H<sub>2</sub>) min<sup>-1</sup> for over 100 min. After completion of the reaction, we examined the postused fuel solution by UV–vis spectroscopy (Figure S11, Supporting Information). The invisibility of the N<sub>2</sub>H<sub>4</sub>·H<sub>2</sub>O signal in UV–vis spectroscopy analysis clearly indicated a 100% fuel conversion. In particular, the thus-constituted system yielded a hydrogen capacity as high as 6.28 wt %.

The dynamic response property to the varied hydrogen demands is also a key parameter for practical H<sub>2</sub> source systems. In the present work, we tested the dynamic response performance of the N<sub>2</sub>H<sub>4</sub>·H<sub>2</sub>O-based HP system by periodi-

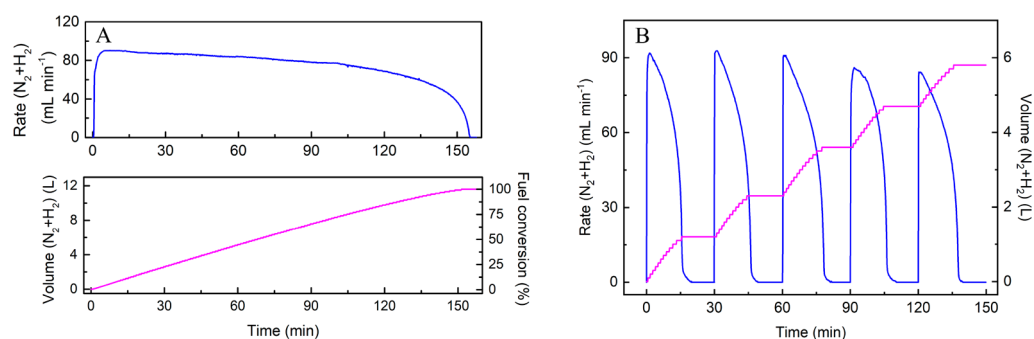


**Figure 7.** Kinetic curves of concentrated  $N_2H_4 \cdot H_2O$  decomposition over the  $400^\circ C$ -reduced catalyst at  $50^\circ C$ . (A) Time course profiles of 10 mL concentrated  $N_2H_4 \cdot H_2O$  decomposition reaction rate (top) and fuel conversion (bottom) (B) Start/stop hydrogen production dynamics profile of 1 mL concentrated  $N_2H_4 \cdot H_2O$  decomposition. (System composition: 17.5 M  $N_2H_4 \cdot H_2O$  + 2 M NaOH + 400 mg of catalyst.)

cally feeding the fuel solution into the reactor with preloaded  $Ni_4W/WO_2/NiWO_4$  catalyst. As shown in Figure 7B, the catalytic decomposition reaction of  $N_2H_4 \cdot H_2O$  immediately occurred upon contacting the fuel solution with the catalyst, and importantly, the system rapidly reached the maximum rate within  $\sim 1$  min and completed the HP process within approximately 20 min for each start/stop cycle test. Examination of the kinetics profiles found that the maximum reaction rates decreased slightly with increasing the cycle number, which might be attributed to the dilution of the  $N_2H_4 \cdot H_2O$  fuel solution by the water byproduct from the previous cycle. Evidently, a favorable combination of high hydrogen capacity, rapid dynamic response, and stable HP performance of the present  $Ni_4W/WO_2/NiWO_4$  composite catalyst may lay foundation for the practical applications of the  $N_2H_4 \cdot H_2O$ -based  $H_2$  source system.

## CONCLUSIONS

The Ni–W–O-derived nanocomposite catalysts can be readily synthesized by a hydrothermal process in combination with reductive annealing treatment. Depending upon the annealing temperature, the thus-prepared catalysts exhibited remarkably distinct catalytic performances toward  $N_2H_4 \cdot H_2O$  decomposition regarding both activity and  $H_2$  selectivity. On the basis of a combination of phase/microstructure/chemical state analyses and DFT theoretical calculations, the observed catalytic property changes can be correlated with the temperature-dependent evolutions of phase structure and microstructural features of the catalyst in the reductive annealing process. Our study revealed that the phase constitution and distribution state of Ni–W alloys played important roles in the catalytic performance toward  $N_2H_4 \cdot H_2O$  decomposition. Specifically, a  $Ni_4W/WO_2/NiWO_4$  nanocomposite catalyst showed high activity, nearly 100% selectivity, and exceptionally high stability toward  $N_2H_4 \cdot H_2O$  decomposition for hydrogen production. Using this noble-metal-free catalyst, we have developed a  $N_2H_4 \cdot H_2O$ -based hydrogen production system with a material-based hydrogen capacity as high as 6.28 wt % and rapid dynamic response property. Our study could enlighten and encourage future exploration of catalytic decomposition of  $N_2H_4 \cdot H_2O$  as a practical on-demand hydrogen production technology for mobile and portable applications.

## ASSOCIATED CONTENT

### Supporting Information

The Supporting Information is available free of charge at <https://pubs.acs.org/doi/10.1021/acssuschemeng.9b07782>.

Computational models of Ni–W alloys and  $N_2H_4$  adsorption conformations on the catalyst surfaces, XRD patterns and Raman spectra of the reduced samples, kinetic curves of the catalysts with different Ni/W molar ratios,  $N_2$  adsorption/desorption isotherms and pore size distribution curves, performance dependence of the catalyst on annealing temperature or annealing time, XRD patterns and TEM images of the catalyst before and after stability test, UV–vis spectra of the postused hydrous hydrazine solution, and table showing a comparison of catalytic performances of noble-metal-free catalysts (PDF)

## AUTHOR INFORMATION

### Corresponding Author

**Ping Wang** – School of Materials Science and Engineering, South China University of Technology, Guangzhou 510641, P.R. China; [orcid.org/0000-0002-7704-2538](https://orcid.org/0000-0002-7704-2538); Phone: +86 20 3938 0583; Email: [mbspwang@scut.edu.cn](mailto:mbspwang@scut.edu.cn)

### Authors

**Qing Shi** – School of Materials Science and Engineering, South China University of Technology, Guangzhou 510641, P.R. China

**Deng-Xue Zhang** – School of Materials Science and Engineering, South China University of Technology, Guangzhou 510641, P.R. China

**Hui Yin** – School of Materials Science and Engineering, South China University of Technology, Guangzhou 510641, P.R. China

**Yu-Ping Qiu** – School of Materials Science and Engineering, South China University of Technology, Guangzhou 510641, P.R. China

**Liang-Liang Zhou** – School of Materials Science and Engineering, South China University of Technology, Guangzhou 510641, P.R. China

**Chen Chen** – School of Materials Science and Engineering, South China University of Technology, Guangzhou 510641, P.R. China

**Hui Wu** – NIST Center for Neutron Research, National Institute of Standards and Technology, Gaithersburg, Maryland 20899-6102, United States; [orcid.org/0000-0003-0296-5204](https://orcid.org/0000-0003-0296-5204)

Complete contact information is available at:  
<https://pubs.acs.org/10.1021/acssuschemeng.9b07782>

## Notes

The authors declare no competing financial interest.

## ACKNOWLEDGMENTS

This work was supported by the National Key R&D Program of China (2018YFB1502104), the National Natural Science Foundation of China (51671087 and 51621001), and the Natural Science Foundation of Guangdong Province (2016A030312011).

## REFERENCES

- (1) Schlapbach, L.; Züttel, A. Hydrogen-storage materials for mobile applications. *Nature* **2001**, *414* (6861), 353–358.
- (2) Sandrock, G.; Suda, S.; Schlapbach, L. Hydrogen in intermetallic compounds II. *Top. Appl. Phys.* **1992**, *67* (5), 197–258.
- (3) Orimo, S. I.; Nakamori, Y.; Eliseo, J. R.; et al. Complex hydrides for hydrogen storage. *Chem. Rev.* **2007**, *107* (10), 4111–4132.
- (4) Suh, M. P.; Park, H. J.; Prasad, T. K.; et al. Hydrogen storage in metal-organic frameworks. *Chem. Rev.* **2012**, *112* (2), 782–835.
- (5) Hirscher, M.; Autrey, T.; Orimo, S. I. Hydrogen energy. *ChemPhysChem* **2019**, *20* (10), 1157–1157.
- (6) Dagdougui, H.; Sacile, R.; Bersani, C.; et al. *Hydrogen infrastructure for energy applications: Implementation scenarios*; Academic Press: 2018; pp 37–52, DOI: 10.1016/B978-0-12-812036-1.00004-4.
- (7) Preuster, P.; Alekseev, A.; Wasserscheid, P. Hydrogen storage technologies for future energy systems. *Annu. Rev. Chem. Biomol. Eng.* **2017**, *8*, 445–471.
- (8) Yartys, V. A.; Lototskyy, M. V.; Akiba, E.; et al. Magnesium based materials for hydrogen based energy storage: past, present and future. *Int. J. Hydrogen Energy* **2019**, *44* (15), 7809–7859.
- (9) Milanese, C.; Jensen, T. R.; Hauback, B. C.; et al. Complex hydrides for energy storage. *Int. J. Hydrogen Energy* **2019**, *44* (15), 7860–7874.
- (10) Paskevicius, M.; Jepsen, L. H.; Schouwink, P.; et al. Metal borohydrides and derivatives—synthesis, structure and properties. *Chem. Soc. Rev.* **2017**, *46* (5), 1565–1634.
- (11) Kumar, R.; Karkamkar, A.; Bowden, M.; et al. Solid-state hydrogen rich boron–nitrogen compounds for energy storage. *Chem. Soc. Rev.* **2019**, *48* (21), 5350–5380.
- (12) Hansen, B. R. S.; Paskevicius, M.; Li, H.-W.; et al. Metal boranes: Progress and applications. *Coord. Chem. Rev.* **2016**, *323* (15), 60–70.
- (13) Møller, K. T.; Sheppard, D.; Ravnsbæk, D. B.; et al. Complex metal hydrides for hydrogen, thermal and electrochemical energy storage. *Energies* **2017**, *10* (10), 1645–1675.
- (14) Zhu, Q. L.; Xu, Q. Liquid organic and inorganic chemical hydrides for high-capacity hydrogen storage. *Energy Environ. Sci.* **2015**, *8* (2), 478–512.
- (15) Demirci, U. B.; Miele, P. Chemical hydrogen storage: ‘material’ gravimetric capacity versus ‘system’ gravimetric capacity. *Energy Environ. Sci.* **2011**, *4* (9), 3334–3341.
- (16) Schmidt, E. W. *Hydrazine and its derivatives. preparation, properties, applications*, 2nd ed.; John Wiley & Sons: New York, 2001.
- (17) Yadav, M.; Xu, Q. Liquid-phase chemical hydrogen storage materials. *Energy Environ. Sci.* **2012**, *5* (12), 9698–9725.
- (18) Cho, S. J.; Lee, J.; Lee, Y. S.; et al. Characterization of iridium catalyst for decomposition of hydrazine hydrate for hydrogen generation. *Catal. Lett.* **2006**, *109* (3–4), 181–187.
- (19) Singh, S. K.; Zhang, X. B.; Xu, Q. Room-temperature hydrogen generation from hydrous hydrazine for chemical hydrogen storage. *J. Am. Chem. Soc.* **2009**, *131* (29), 9894–9895.
- (20) Singh, S. K.; Xu, Q. Complete conversion of hydrous hydrazine to hydrogen at room temperature for chemical hydrogen storage. *J. Am. Chem. Soc.* **2009**, *131* (50), 18032–18033.
- (21) Singh, S. K.; Yadav, M.; Aranishi, K.; et al. Temperature-induced selectivity enhancement in hydrogen generation from Rh-Ni nanoparticle-catalyzed decomposition of hydrous hydrazine. *Int. J. Hydrogen Energy* **2012**, *37* (24), 18915–18919.
- (22) Singh, S. K.; Xu, Q. Bimetallic Ni-Pt nanocatalysts for selective decomposition of hydrazine in aqueous solution to hydrogen at room temperature for chemical hydrogen storage. *Inorg. Chem.* **2010**, *49* (13), 6148–6152.
- (23) Singh, S. K.; Iizuka, Y.; Xu, Q. Nickel-palladium nanoparticle catalyzed hydrogen generation from hydrous hydrazine for chemical hydrogen storage. *Int. J. Hydrogen Energy* **2011**, *36* (18), 11794–11801.
- (24) Singh, S. K.; Xu, Q. Bimetallic nickel-iridium nanocatalysts for hydrogen generation by decomposition of hydrous hydrazine. *Chem. Commun.* **2010**, *46* (35), 6545–6547.
- (25) Singh, S. K.; Singh, A. K.; Aranishi, K.; et al. Noble-metal-free bimetallic nanoparticle-catalyzed selective hydrogen generation from hydrous hydrazine for chemical hydrogen storage. *J. Am. Chem. Soc.* **2011**, *133* (49), 19638–19641.
- (26) He, L.; Huang, Y.; Wang, A.; et al. A noble-metal-free catalyst derived from Ni-Al hydroxalite for hydrogen generation from N<sub>2</sub>H<sub>4</sub>·H<sub>2</sub>O decomposition. *Angew. Chem., Int. Ed.* **2012**, *51* (25), 6191–6194.
- (27) Zhang, J.; Kang, Q.; Yang, Z.; et al. A cost-effective NiMoB-La(OH)<sub>3</sub> catalyst for hydrogen generation from decomposition of alkaline hydrous hydrazine solution. *J. Mater. Chem. A* **2013**, *1* (38), 11623–11628.
- (28) Jiang, Y. Y.; Kang, Q.; Zhang, J.; et al. High-performance nickel-platinum nanocatalyst supported on mesoporous alumina for hydrogen generation from hydrous hydrazine. *J. Power Sources* **2015**, *273*, 554–560.
- (29) Jiang, Y. Y.; Dai, H. B.; Zhong, Y. J.; et al. Complete and rapid conversion of hydrazine monohydrate to hydrogen over supported Ni-Pt nanoparticles on mesoporous ceria for chemical hydrogen storage. *Chem. - Eur. J.* **2015**, *21* (43), 15439–15445.
- (30) Dai, H.; Dai, H. B.; Zhong, Y. J.; et al. Kinetics of catalytic decomposition of hydrous hydrazine over CeO<sub>2</sub>-supported bimetallic Ni-Pt nanocatalysts. *Int. J. Hydrogen Energy* **2017**, *42* (9), 5684–5693.
- (31) He, L.; Huang, Y.; Liu, X. Y.; et al. Structural and catalytic properties of supported Ni-Ir alloy catalysts for H<sub>2</sub> generation via hydrous hydrazine decomposition. *Appl. Catal., B* **2014**, *147*, 779–788.
- (32) Wang, J.; Zhang, X. B.; Wang, Z. L.; et al. Rhodium-nickel nanoparticles grown on graphene as highly efficient catalyst for complete decomposition of hydrous hydrazine at room temperature for chemical hydrogen storage. *Energy Environ. Sci.* **2012**, *5* (5), 6885–6888.
- (33) Du, X.; Liu, C.; Du, C.; et al. Nitrogen-doped graphene hydrogel-supported NiPt-CeO<sub>x</sub> nanocomposites and their superior catalysis for hydrogen generation from hydrazine at room temperature. *Nano Res.* **2017**, *10* (8), 2856–2865.
- (34) He, L.; Liang, B.; Li, L.; et al. Cerium-oxide-modified nickel as a non-noble metal catalyst for selective decomposition of hydrous hydrazine to hydrogen. *ACS Catal.* **2015**, *5* (3), 1623–1628.
- (35) Kang, W.; Varma, A. Hydrogen generation from hydrous hydrazine over Ni/CeO<sub>2</sub> catalysts prepared by solution combustion synthesis. *Appl. Catal., B* **2018**, *220*, 409–416.
- (36) Fu, Q.; Yang, P.; Wang, J.; et al. In situ synthesis of Ni nanofibers via vacuum thermal reduction and their efficient catalytic properties for hydrogen generation. *J. Mater. Chem. A* **2018**, *6* (24), 11370–11376.
- (37) Kang, W.; Guo, H.; Varma, A. Noble-metal-free NiCu/CeO<sub>2</sub> catalysts for H<sub>2</sub> generation from hydrous hydrazine. *Appl. Catal., B* **2019**, *249*, 54–62.
- (38) Qiu, Y. P.; Cao, G. X.; Wen, H.; et al. High-capacity hydrogen generation from hydrazine monohydrate using a noble-metal-free

Ni<sub>10</sub>Mo/Ni-Mo-O nanocatalyst. *Int. J. Hydrogen Energy* **2019**, *44* (29), 15110–15117.

(39) Wang, K.; Yao, Q.; Qing, S.; et al. La(OH)<sub>3</sub> nanosheet-supported CoPt nanoparticles: a highly efficient and magnetically recyclable catalyst for hydrogen production from hydrazine in aqueous solution. *J. Mater. Chem. A* **2019**, *7* (16), 9903–9911.

(40) Shi, Q.; Qiu, Y. P.; Dai, H.; et al. Study of formation mechanism of Ni-Pt/CeO<sub>2</sub> catalyst for hydrogen generation from hydrous hydrazine. *J. Alloys Compd.* **2019**, *787*, 1187–1194.

(41) Wan, C.; Sun, L.; Xu, L.; et al. Novel NiPt alloy nanoparticle decorated 2D layered g-C<sub>3</sub>N<sub>4</sub> nanosheets: a highly efficient catalyst for hydrogen generation from hydrous hydrazine. *J. Mater. Chem. A* **2019**, *7* (15), 8798–8804.

(42) Dai, H.; Zhong, Y.; Wang, P. Hydrogen generation from decomposition of hydrous hydrazine over Ni-Ir/CeO<sub>2</sub> catalyst. *Prog. Nat. Sci.* **2017**, *27* (1), 121–125.

(43) Wu, D.; Wen, M.; Gu, C.; et al. 2D NiFe/CeO<sub>2</sub> basic-site-enhanced catalyst via in-situ topotactic reduction for selectively catalyzing the H<sub>2</sub> generation from N<sub>2</sub>H<sub>4</sub>·H<sub>2</sub>O. *ACS Appl. Mater. Interfaces* **2017**, *9* (19), 16103–16108.

(44) Wu, D.; Wen, M.; Lin, X.; Wu, Q.; Gu, C.; Chen, H. A NiCo/NiO–CoO<sub>x</sub> ultrathin layered catalyst with strong basic sites for high-performance H<sub>2</sub> generation from hydrous hydrazine. *J. Mater. Chem. A* **2016**, *4* (17), 6595–6602.

(45) Men, Y.; Du, X.; Cheng, G.; Luo, W.; et al. CeO<sub>x</sub>-modified NiFe nanodendrites grown on rGO for efficient catalytic hydrogen generation from alkaline solution of hydrazine. *Int. J. Hydrogen Energy* **2017**, *42* (44), 27165–27173.

(46) Wang, H. L.; Yan, J. M.; Li, S. J.; et al. Noble-metal-free NiFeMo nanocatalyst for hydrogen generation from the decomposition of hydrous hydrazine. *J. Mater. Chem. A* **2015**, *3* (1), 121–124.

(47) Dai, H.; Qiu, Y. P.; Dai, H. B.; et al. A study of degradation phenomenon of Ni-Pt/CeO<sub>2</sub> catalyst towards hydrogen generation from hydrous hydrazine. *Int. J. Hydrogen Energy* **2017**, *42* (26), 16355–16361.

(48) Kresse, G.; Furthmüller, J. Efficient iterative schemes for ab initio total-energy calculations using a plane-wave basis set. *Phys. Rev. B: Condens. Matter Mater. Phys.* **1996**, *54* (16), 11169–11186.

(49) Perdew, J. P.; Burke, K.; Ernzerhof, M. Generalized gradient approximation made simple. *Phys. Rev. Lett.* **1996**, *77* (18), 3865–3868.

(50) Blöchl, P. E. Projector augmented-wave method. *Phys. Rev. B: Condens. Matter Mater. Phys.* **1994**, *50* (24), 17953–17979.

(51) Grimme, S. Semiempirical GGA-type density functional constructed with a long-range dispersion correction. *J. Comput. Chem.* **2006**, *27* (15), 1787–1799.

(52) Bučko, T.; Hafner, J.; Lebègue, S.; et al. Improved description of the structure of molecular and layered crystals: ab initio DFT calculations with van der Waals corrections. *J. Phys. Chem. A* **2010**, *114* (43), 11814–11824.

(53) Xing, X.; Wang, J. Reduced graphene oxide incorporated NiWO<sub>4</sub> for high-performance energy storage. *J. Mater. Sci.: Mater. Electron.* **2016**, *27* (11), 11613–11622.

(54) Xu, X.; Pei, L.; Yang, Y.; et al. Facile synthesis of NiWO<sub>4</sub>/reduced graphene oxide nanocomposite with excellent capacitive performance for supercapacitors. *J. Alloys Compd.* **2016**, *654*, 23–31.

(55) Cao, G. X.; Chen, Z. J.; Yin, H.; et al. Investigation of the correlation between the phase structure and activity of Ni–Mo–O derived electrocatalysts for the hydrogen evolution reaction. *J. Mater. Chem. A* **2019**, *7* (17), 10338–10345.

(56) Tang, H.; Trout, B. L. NO chemisorption on Pt(111), Rh/Pt(111), and Pd/Pt(111). *J. Phys. Chem. B* **2005**, *109* (37), 17630–17634.

(57) Majerz, I.; Olovsson, I. Comparison of the proton-transfer paths in hydrogen bonds from theoretical potential-energy surfaces and the concept of conservation of bond order III. O–H–O hydrogen bonds. *Phys. Chem. Chem. Phys.* **2010**, *12* (20), 5462–5467.

(58) Zhang, P. X.; Wang, Y. G.; Huang, Y. Q.; et al. Density functional theory investigations on the catalytic mechanisms of hydrazine decompositions on Ir (111). *Catal. Today* **2011**, *165* (1), 80–88.

(59) Deng, Z.; Lu, X.; Wen, Z.; et al. Mechanistic insight into the hydrazine decomposition on Rh (111): effect of reaction intermediate on catalytic activity. *Phys. Chem. Chem. Phys.* **2013**, *15* (38), 16172–16182.

(60) Yin, H.; Qiu, Y. P.; Dai, H.; et al. Understanding of selective H<sub>2</sub> generation from hydrazine decomposition on Ni (111) Surface. *J. Phys. Chem. C* **2018**, *122* (10), 5443–5451.